Rare Met. (2022) 41(7):2439–2452
https://doi.org/10.1007/s12598-022-01984-5

RARE METALS

ORIGINAL ARTICLE

Ultrafast photocatalytic degradation of nitenpyram by 2D ultrathin Bi_2WO_6: mechanism, pathways and environmental factors

Yuan-Hao Cheng, Juan Chen, Hui-Nan Che, Yan-Hui Ao*, Bin Liu

Received: 5 November 2021 / Revised: 15 December 2021 / Accepted: 22 December 2021 / Published online: 19 April 2022

Abstract As a common insecticide, nitenpyram (NTP) seriously threatens the human health and environmental safety. In this work, a visible-light-responsive photocatalyst two-dimensional (2D) Bi_2WO_6 was synthesized and applied to degrade NTP. Compared with bulk Bi_2WO_6, the 2D Bi_2WO_6 exhibits better photocatalytic performance for NTP degradation under visible-light irradiation. The enhanced activity can be ascribed to the unique 2D structure which would induce to higher efficiency of carrier separation. Moreover, hole (h^+) plays a major role (and $\cdot O_2^-$) in the degradation of NTP. Based on the intermediates detected by high-performance liquid chromatography–mass spectrometry (HPLC–MS), the degradation pathway of NTP was proposed. In addition, the influence of typical environmental factors (pH, water matrix, inorganic cations and common anions) on the degradation of NTP was also investigated. This work not only helps people to understand the degradation of pesticides in actual water bodies, but also provides reference for the subsequent treatment of agricultural wastewater.

Keywords Photocatalysis; Two-dimensional (2D) Bi_2WO_6; Nitenpyram; Degradation pathway

1 Introduction

The water pollution caused by pesticide using has always been a serious problem getting more and more concerns recently [1–3]. Massive pesticides residual in the farmlands are mainly collected into natural water bodies and further cause adverse influence on the human health and environment [4–6]. Nitenpyram (NTP), based on its high efficiency, systemic pest control and non-interaction, becomes one of the commonly used neonicotinoid pesticides [7]. Despite the above-mentioned advantages, the solubility of nitenpyram in water is very high, up to 590 $g \cdot L^{-1}$ [8]. Thus, as the rain washes, NTP residual on the farmlands easily migrates to the soil and water bodies [9]. Additionally, the soluble NTP appears particularly hard to adsorb and degrade in the water bodies. Except for the aforesaid study, research reports have shown that non-degradable NTP disrupts the ecology by the use of affecting bee pollination and the intestinal health community structure of pregnant mice [10, 11]. Traditional methods currently used to treat nitenpyram include plant microbial methods, physical adsorption methods and electrochemical methods [12–14]. However, on account of treatment effects, cost and recyclability, these methods mostly cannot be widely used. Therefore, there is an urgent need for an environmental, friendly and low-cost way to degrade NTP in the aquatic environment. Photocatalytic degradation of pollutants in the water environment has attracted much attention because of its sustainable development strategy and good application prospect [15–20].

Yuan-Hao Cheng and Juan Chen contributed equally to this work.

Supplementary Information The online version contains supplementary material available at https://doi.org/10.1007/s12598-022-01984-5.

Y.-H. Cheng, J. Chen, H.-N. Che, Y.-H. Ao*
Key Laboratory of Integrated Regulation and Resource Development on Shallow Lakes of Ministry of Education, College of Environment, Hohai University, Nanjing 210098, China
e-mail: andyao@hhu.edu.cn

B. Liu
School of Chemical and Biomedical Engineering, Nanyang Technological University, Singapore 637459, Singapore

Bismuth tungstate (Bi_2WO_6), as a kind of Aurivillius compound, is known as an efficient, active and stable photocatalyst [21, 22]. Because of its unique orthogonal structure (consisting of alternating WO_4 octahedral layers and Bi-O-Bi composite layers) [23], open structure of Bi_2WO_6 nowadays attracts more and more attention due to its usage as photocatalytic active sites. This material is also visible-light-responsive, stable and controllable of its shape. However, its performance is adversely affected by its fast photogenerated carries recombination and fewer active sites for pollutions. For long, many works have been reported to improve the photocatalytic performance of Bi_2WO_6 [21, 24–27]. Many methods such as changing morphology [28], oxygen vacancy construction [29, 30], metal doping [31] and heterojunction engineering [32–35] were used to improve photocatalytic performance. Especially, the heterojunction system of layered materials can greatly improve photocatalytic performance [36]. Compared with single catalyst, the visible-light response and the photogenerated carrier rate are simultaneously improved. It was reported that the 2D/2D CsPbBr/Bi_2WO_6 heterojunction synthesized by electrostatic self-assembly technology has extremely fast charge transfer speed, thus highly improving the photocatalytic reduction of CO_2 [37]. NH_2MIL-125(Ti)/Bi_2WO_6 composite material which is also synthesized by electrostatic self-assembly possesses suitable bandgap because of Bi_2WO_6. Moreover, this photocatalyst can highly improve carrier separation and excellently degrade organic pollutants [36]. However, for Bi_2WO_6 layered material, the structure of the composite material will affect its morphology and surface-active sites [38]. Thus, the construction of two-dimensional (2D) nanomaterials can significantly improve the photocatalytic performance of the material because of the heterojunction-like structure between the double layers. In short, this has a strong application prospect [27, 39].

During the photocatalytic degradation of pollutants, we often pay more attention to the intermediate product of the reaction process and propose the corresponding degradation path according to the results of the characterization. For NTP, some studies have shown that photocatalyst can degrade it very rapidly, and the corresponding reaction mechanism and possible degradation path have been proposed [40]. But the intermediation in the reaction may cause greater harm to the environment than the original pollutants. Furthermore, in practical applications, pH, common ion influence and water types all affect the photocatalytic reaction. However, there are few studies on the impact of water environmental factors on the photocatalytic degradation of NTP and the possible environmental risk caused by reaction intermediates.

In this work, ultrathin 2D bismuth tungstate nanosheets (2D Bi_2WO_6) were synthesized and applied to degrade NTP. The degradation principle of nitenpyram was analyzed, including the main active substances, principles and intermediate products of the reaction. Ultimately, we also studied the effects of common water environmental factors on the degradation reaction of nitenpyram (pH, common anions, common cations and water matrix).

2 Experimental

2.1 Preparation of 2D Bi_2WO_6 and bulk Bi_2WO_6

2D Bi_2WO_6 was synthesized as follows. 1 mmol $Na_2WO_4{\cdot}2H_2O$ and 50 mg cetyltrimethylammonium bromide (CTAB) were added to 80 ml deionized water. The mixture was stirred until there is no solid in the solution, and then, 2 mmol $Bi(NO_3)_3{\cdot}5H_2O$ was added to the solution and stirred with a magnetic stirrer. The above solution was transferred to a 100-ml reactor and heated at 120 °C for 24 h. Finally, the obtained sample was washed 5 times with deionized water and then washed 2 times with absolute ethanol and dried at 60 °C for 10 h.

Bulk bismuth tungstate (bulk Bi_2WO_6) was compounded by the hydrothermal method, and the only difference from the synthesis of 2D Bi_2WO_6 is that CTAB is not added.

2.2 Characterization

X-ray diffraction (XRD, Rigaku, SmartLab) was used to test and analyze phase purity and crystallinity of the prepared samples. The scanning range was 2θ = 10°–90°, the scanning speed was 7 (°)·min^{-1}, and the step size was 0.02°. The morphology and microstructure were observed and analyzed by transmission electron microscope (TEM, JEOL, JEM-2100 (HR)). X-ray photoelectron spectra (XPS) was recorded by Thermo ESCALAB 250 with Al Kα X-ray. The optical properties of the obtained samples were measured by an ultraviolet–visible spectrophotometer (Shimadzu, UV-3600), and the photoluminescence spectrum was measured by a fluorescence spectrophotometer (PL, Hitachi, F-7000). During the test, an external dual detector was used with a slit width of 20 nm, barium sulfate ($BaSO_4$) was used as a reference, and the scanning range was from 200 to 800 nm.

2.3 Photocatalytic studies

Under visible-light irradiation, the photocatalysis experiment was carried out in pure water with a natural pH of 7. 25 mg catalyst and 50 ml (5×10^{-6}) nitenpyram were

added into the beaker and stirred for 30 min in the dark, the 0 min point was taken, and then it was irradiated under a 300-W lamp ($\lambda > 420$ nm) light reaction for 10 min. After filtration, the concentration of nitenpyram in the samples was determined by high-performance liquid chromatography (Waters e2695, the liquid chromatograph conditions are: column temperature of 26 °C, C_{18} column, mobile phase: 60% water + 40% acetonitrile, flow rate of 1 ml·min^{-1}).

2.4 Photochemical characterization

The photoelectric response performance of the synthesized sample, including photocurrent and electrochemical impedance, can be measured by an electrochemical workstation (Shanghai Chenhua Instrument, CHI660D). The standard three-electrode system was used, namely the sample membrane, Ag/AgCl electrode and platinum electrode, corresponded to the working electrode, reference electrode and counter electrode, respectively. The electrolyte was a 0.1 mol·L^{-1} sodium sulfate (Na_2SO_4) solution, and the visible-light source was 250-W mercury lamp (Zhongjiao Jinyuan) provided. The sample film was prepared by the following steps: 20 mg photocatalyst was dissolved in 1.5 ml absolute ethanol and 20 μl naphthol was added, and then the resulting uniform liquid was coated on a 1-cm^2 conductive glass (FTO), and then waiting for it after natural air drying, it was transferred to an oven and calcined at 150 °C for 2 h to prevent falling off during the experiment.

3 Results and discussion

3.1 Characterization

XRD results of the synthesized samples are shown in Fig. 1. For two samples, 2θ pattern has characteristic peaks at 28.3°, 32.8°, 47.1°, 55.8°, 58.7°, 68.8°, 76.1° and 78.2°,

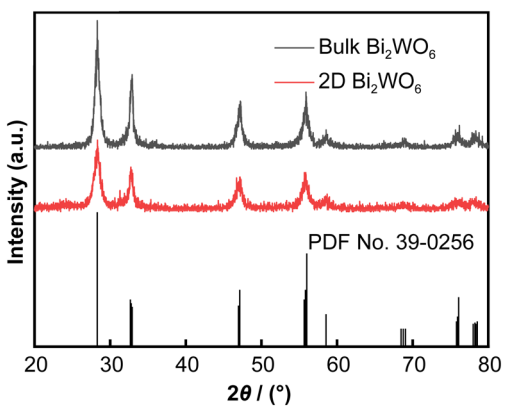

Fig. 1 XRD patterns of 2D Bi_2WO_6 and bulk Bi_2WO_6

corresponding to (131), (002), (202), (331), (262), (262), (391) and (460) planes of orthorhombic Bi_2WO_6 phase (JCPDS No. 39-0256). The above result indicates that the Bi_2WO_6 sample was successfully synthesized [41–43]. In addition, the two synthetic materials have no other peaks, indicating that the synthesized 2D Bi_2WO_6 and bulk Bi_2WO_6 have high purity and no other impurities are introduced. Besides, the morphologies of samples were tested by TEM and high-resolution TEM (HRTEM). In Fig. 2a, c, 2D Bi_2WO_6 is evenly laid out in flakes and less agglomerated, indicating that we successfully synthesized the lamellar Bi_2WO_6. Figure 2b shows its HRTEM image. It is not difficult to find that the sample has good crystallization properties. The Gatan digital micrograph was used to analyze it, and the interplanar spacing of 2D Bi_2WO_6 was measured to be 0.273 nm, corresponding to the crystal surface (200) of Bi_2WO_6. As present in TEM images of bulk Bi_2WO_6 (Fig. 2d, e), the bulk Bi_2WO_6 shows more serious agglomeration, compared with 2D Bi_2WO_6. As shown in HRTEM image of bulk bismuth tungstate (Fig. 2f), compared with 2D Bi_2WO_6, the accumulation is too thick although the crystallinity is still good. TEM analysis can preliminarily show that CTAB as a long-chain molecule can be inserted between the [Bi-O-Bi] layers, thereby reducing stacking and inducing to the ultrathin 2D structure [44]. However, the bulk Bi_2WO_6 does not use CTAB, which shows more serious reunion. From this, the reason we speculate why the 2D Bi_2WO_6 photocatalyst is better than the bulk is due to its single-layer structure. A thinner plane can provide more active sites to adsorb pollutants at the same mass, which further confirms the experimental results of the adsorption dark reaction stage.

Moreover, to further understand the atomic composition of the material, XPS was used to probe. It can be seen that 2D Bi_2WO_6 contains Br in addition to Bi, W and O (Fig. 3a). As shown in Bi 4f spectrum (Fig. 3b), the shoulder peak appears at higher binding energy (Bi $4f_{5/2}$, 164.78 eV; Bi $4f_{7/2}$, 159.27 eV), indicating that a higher positive Bi appears in the monolayer [44]. This indicates that some Bi atoms are bonded with surface Br atoms. Moreover, the binding energy difference between both peaks is about 5.5 eV, which is considered to be Bi^{3+} [45, 46]. Figure 3c shows W 4f spectrum of the sample. It is observed that the two peaks appear at 35.57 and 37.8 eV which are attributed to W $4f_{7/2}$ and W $4f_{7/4}$, respectively. This indicates a valence state of + 6 for tungsten appears and this result is consistent with previous studies of bulk Bi_2WO_6, because the $[WO_4]^{2-}$ layer is located in the middle and is hardly affected by the surface Br atoms [27, 47, 48]. As show in O 1s spectrum (Fig. 3d), two peaks at 529.9 and 530.7 eV are observed. This is attributed to lattice oxygen and bridged hydroxyl groups, respectively. The peak caused by absorption of water was

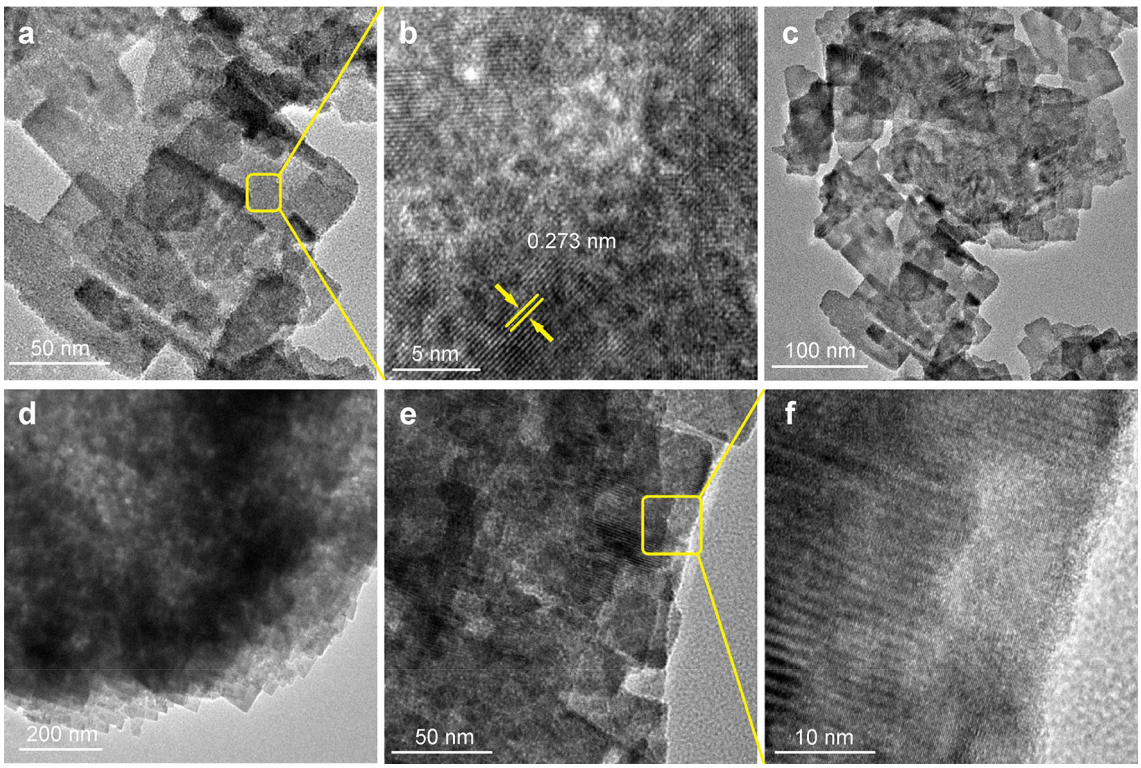

Fig. 2 TEM images of **a–c** 2D Bi_2WO_6 and **d–f** bulk Bi_2WO_6

not detected, indicating that the sample has a certain degree of hydrophobicity which can provide more sites for the adsorption of pollutants [44, 47, 49]. As shown in Fig. 3e, an obvious Br 3d peak appears at 68.6 eV, indicating that the Bi atoms of the monolayer bond with Br^- from CTAB, which corresponds to TEM results.

The application of ultraviolet diffuse reflection can show the optical properties of this material. From Fig. 4a, the absorption edge of 2D Bi_2WO_6 is at $\sim$ 450 nm. The bind energy can be calculated by the following formula [50]:

$$(\alpha hv)^{n/2} = A(hv - E_g) \quad (1)$$

where α, h, v and A are the absorption coefficient, Planck's constant, light frequency and a constant, respectively; E_g is the bind energy. n is related to the type of semiconductor (n = 1 or 4, for a direct or indirect transition, respectively), and the n value of Bi_2WO_6 is 1. The calculated results show that the band gap of both 2D Bi_2WO_6 and bulk Bi_2WO_6 is 2.67 eV (Fig. S1). Put the result into the formula:

$$\lambda_g = 1240/E_g \quad (2)$$

where λ_g is the light-absorbing edge (λ_g = 464.4 nm). Compared with ultraviolet–visible diffuse reflectance spectroscopy, two samples both have well visible-light absorption. Furthermore, the valence band (VB) of 2D Bi_2WO_6 is determined by XPS valence spectrum, as shown in Fig. S2. Combined with the band gap settled above, the valence band and conduction band of 2D Bi_2WO_6 are 2.29 eV (relative to the Fermi level), and $-$ 0.33 eV, respectively.

The PL spectra of pure 2D Bi_2WO_6 and bulk Bi_2WO_6 with an excitation wavelength of 300 nm were measured under a voltage of 700 V to probe the recombination of photogenerated electron–hole charges [51]. For bulk Bi_2WO_6, due to the ultrafast recombination of excited electron–hole pairs, two strong emission peaks can be seen near 469 and 450 nm (Fig. 4b). However, the intensity of 2D Bi_2WO_6 decreased significantly, indicating that the generated electrons migrate to the $[WO_4]^{2-}$ layer in the sandwich structure, thereby inhibiting the recombination of carriers [52]. In the photocatalytic reaction, the carrier transfer efficiency has a great influence on photocatalysis. Therefore, we used the electrochemical workstation to measure the transient photocurrent response (Fig. 4c) of 2D Bi_2WO_6 and bulk Bi_2WO_6 under visible light (the applied voltage was 0.3 V vs. (Ag/AgCl electrode)). As seen, these samples all have obvious responses to the light, but the photocurrent intensities are different. Compared with bulk Bi_2WO_6, the photocurrent intensity of 2D Bi_2WO_6 is significantly improved, which is almost 1.5 times that of bulk Bi_2WO_6. Thus, the charge transfer efficiency is higher. Besides, we also used electrochemical impedance spectroscopy (EIS) to characterize the charge

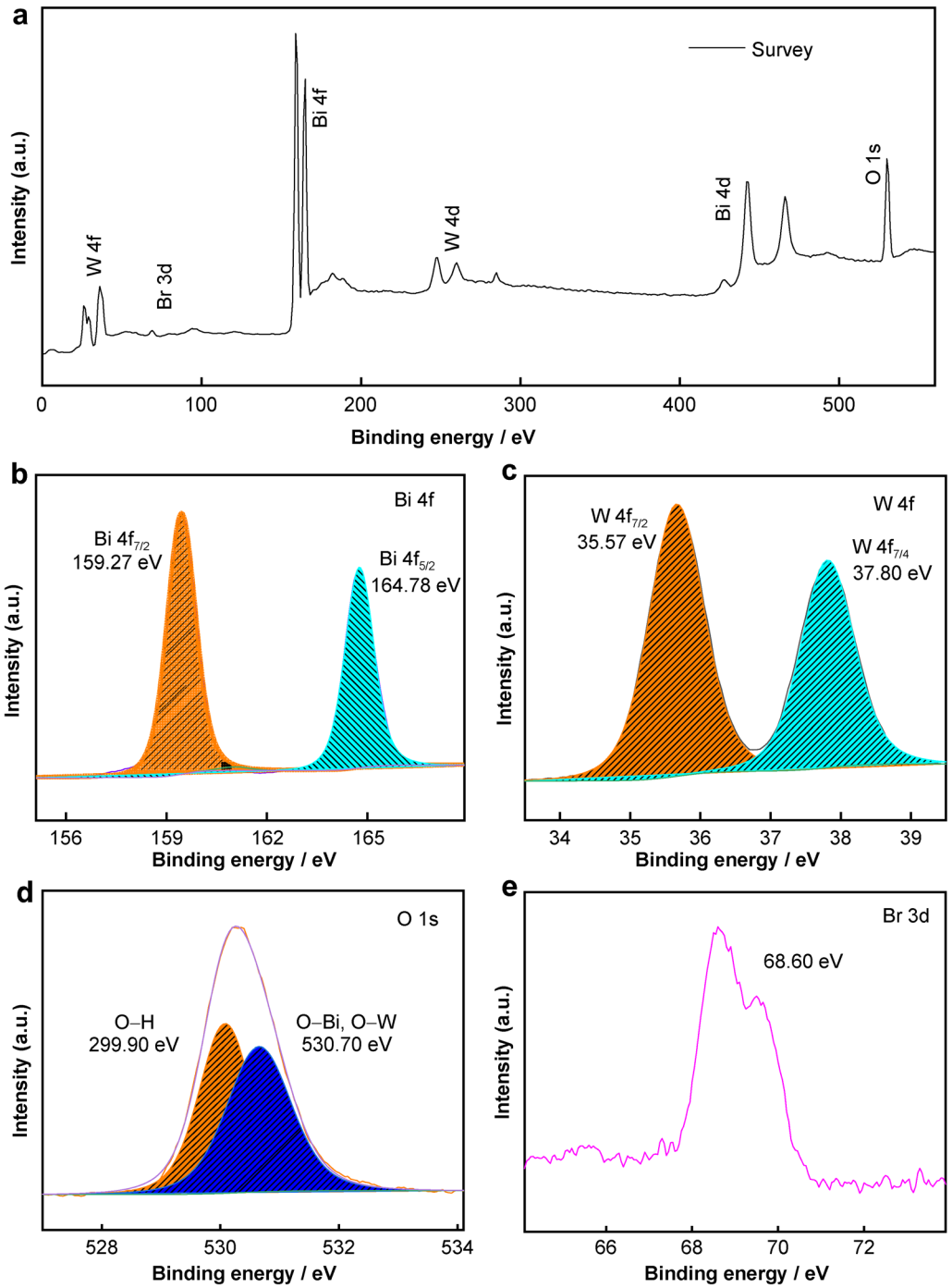

Fig. 3 **a** XPS survey, high-resolution spectra for **b** Bi 4f, **c** W 4f, **d** O 1s and **e** Br 3d of 2D Bi_2WO_6

transfer efficiency of the sample. As shown in Fig. 4d, the radius of 2D Bi_2WO_6 is clearly smaller than that of bulk Bi_2WO_6, which indicates that the layered structure is more helpful for the interface charge transfer of the catalyst.

To reveal the generation of holes and hydroxyl radicals in 2D Bi_2WO_6, the samples were detected by electron spin resonance (ESR). The 2,2,6,6-tetramethylpiperidine-1-oxyl (TEMPO) and 5,5-dimethyl-1-pyrroline N-oxide (DMPO) were used to capture holes (h^+) and hydroxyl radicals (·OH) on the surface of 2D Bi_2WO_6. As shown in Fig. 4e, a quadruple characteristic velocity signal can be observed in the collected ESR spectrum. As the illumination increases, the signal of DMPO-·OH gradually increases, which indicates that photo-induced 2D Bi_2WO_6 generates hydroxyl radicals [53]. In addition, the characteristic triple velocity signal with an intensity of 1:1:1 can be observed in the

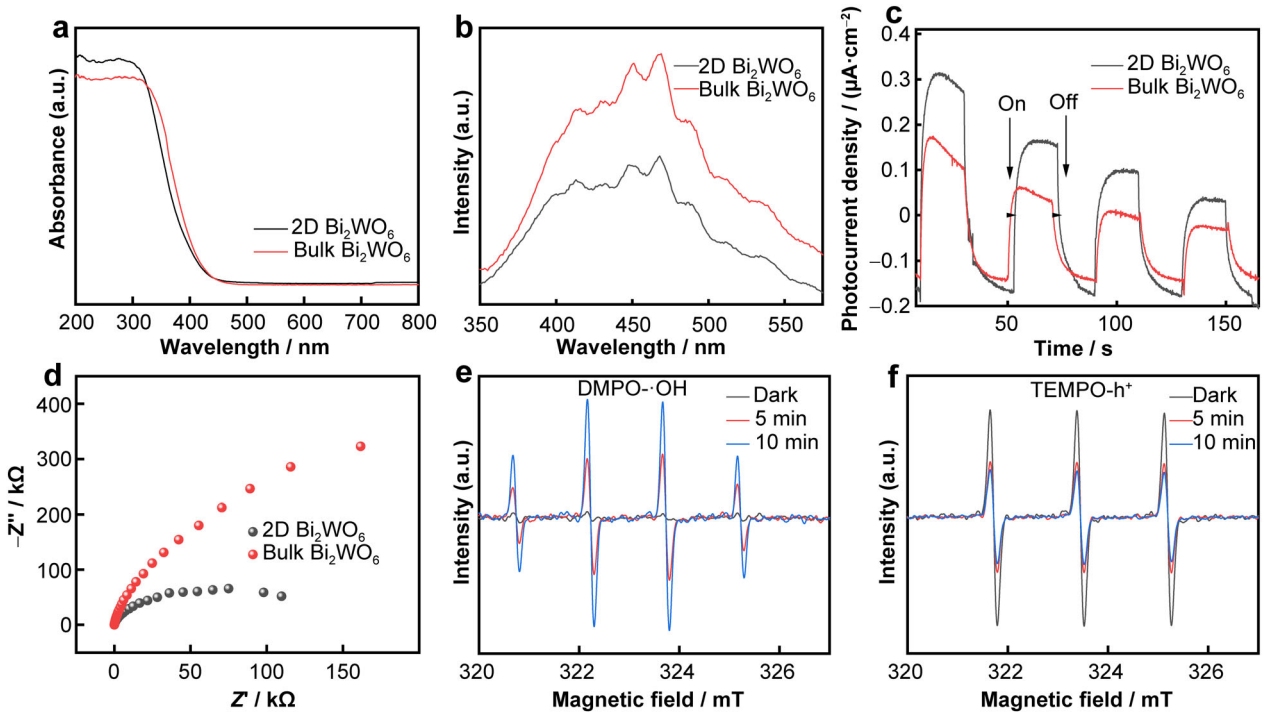

Fig. 4 **a** UV–Vis diffuse reflectance spectroscopy results, **b** PL spectra, **c** photocurrent curves and **d** EIS Nyquist plots of as-prepared samples; ESR diagram of **e** hydroxyl radicals and **f** cavity

collected ESR spectrum (Fig. 4f), and the signal intensity drops sharply with the illumination of visible light. This is because the TEMPO molecule is oxidized to the corresponding oxygen ammonium cation ($TEMPO^+$) by combining with holes in acetonitrile. The reaction is listed [54]:

$$TEMPO + h^+ \rightarrow TEMPO^+ \quad (3)$$

This phenomenon can clearly verify that the optically excited 2D Bi_2WO_6 produces holes. As for the role of these actives substances in the degradation of NTP, it is still not possible to judge.

3.2 Photocatalytic performance and mechanism

As shown in Fig. 5a, there is no photolysis of NTP. The degradation percentages of 2D Bi_2WO_6 on NTP are 94.6% and 25.4% by 2D Bi_2WO_6 and bulk Bi_2WO_6, respectively. To explore the reasons for this phenomenon, we divided the entire reaction process into two stages (dark reaction and light reaction). However, Fig. S3 shows that the concentration of pollution decreased significantly without lighting, which can be attributed to that NTP is adsorbed on the surface of the photocatalyst. The concentration of nitenpyram in the 2D Bi_2WO_6 solution dropped by 49.8%, while that of the bulk Bi_2WO_6 was only 7.8%. This is attributed to that the 2D Bi_2WO_6 has a larger specific surface area, which can provide more adsorption sites for NTP. After the adsorption reached equilibrium, light was added and the degradation of pollution happened in the presence of a photocatalyst. For the photoreaction stage, it is not difficult to find that the degradation ability of 2D Bi_2WO_6 is much stronger than that of bulk one. In order to visually display the nitenpyram degradation ability of different samples, we fitted the degradation kinetic curve through the first-order kinetic equation. The apparent rate constants of different samples are shown in Fig. 5b. The value of 2D Bi_2WO_6 is 0.331 min^{-1}, which is 11.4 times that of bulk Bi_2WO_6. Moreover, we have compared with other work to prove the degradation efficiency of 2D Bi_2WO_6 (Table S1). In summary, compared with bulk Bi_2WO_6, 2D Bi_2WO_6 shows better performance in degrading nitenpyram under visible-light irradiation.

As we all know, photocatalytic reactions involve major active species such as holes, hydroxyl radicals and superoxide radicals. In order to further find out what role active free radicals can play in the degradation process, we carried out capture experiments. Here, 1 mmol isopropanol (IPA) and triethanolamine (TEOA) were added to the degradation system for capturing hydroxyl radicals and holes. Then, the solution was discharged the dissolved oxygen in the solution by introducing argon gas during the experiment [55–57]. Later, by detecting the changes in the degradation reaction of NTP after adding several capture agents, the main active species in the reaction system were further confirmed. As shown in Fig. 5c, d, argon gas and isopropanol all have a significant inhibitory effect on the

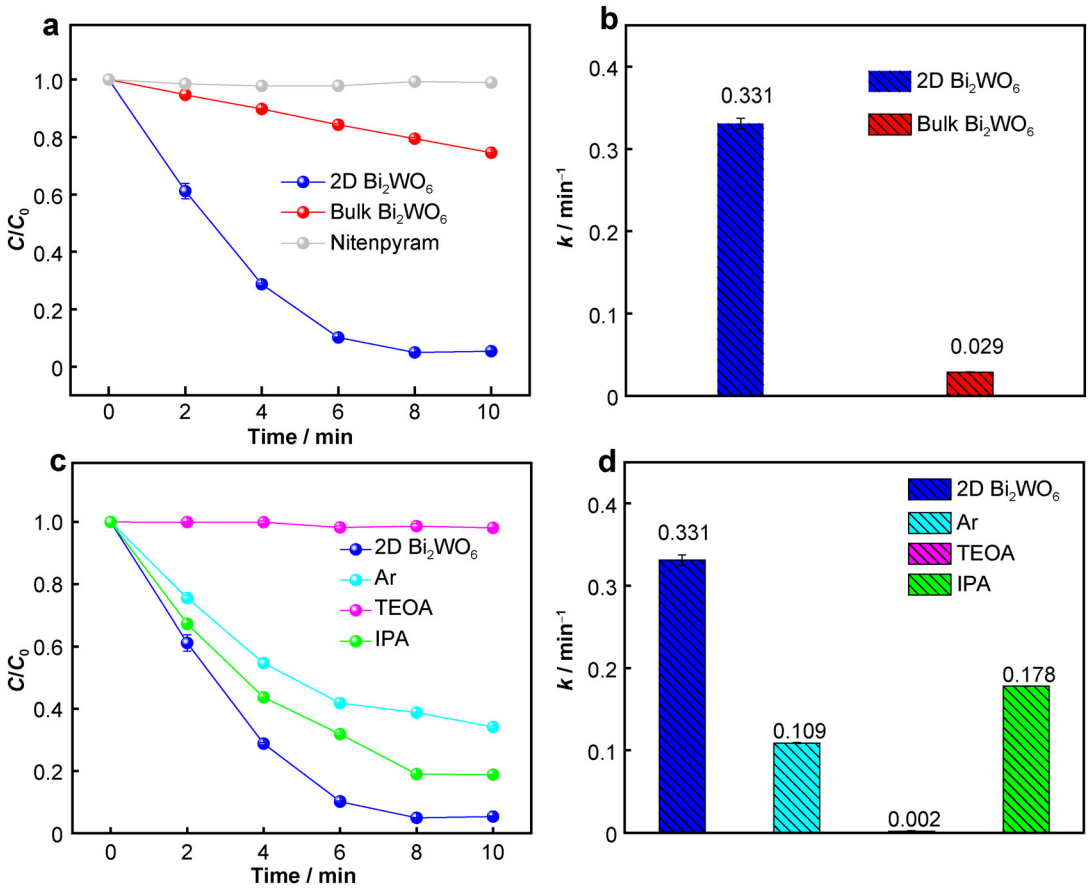

Fig. 5 **a** Degradation curves and **b** rate constants of NTP degradation over different samples; **c** degradation curves and **d** rate constants of NTP degradation under different scavengers for 2D Bi_2WO_6

photocatalytic degradation of nitenpyram. The degradation rate is reduced by 28.7% and 13.4%, respectively, and the kinetic constant (k), respectively, dropped by 0.222 and 0.153 min^{-1}. When TEOA is added, the degradation rate of nitenpyram is only 1.9%, and the kinetic constant (k) is only 0.002 min^{-1}. The above results indicate that in this degradation reaction, holes play a major role (this matches our ESR characterization results). However, ·OH and $\cdot O_2^-$ play a smaller role than h^+ in the degradation of NTP.

Moreover, three-dimensional (3D) EEMs technology was used to deeply understand the NTP process based on 2D Bi_2WO_6. As shown in Fig. 6, four samples were collected under different conditions. It can be seen that with light irradiation, the fluorescence signal first increases because NTP is converted into other substances during the reaction. Subsequently, the fluorescence signal weakens, and nitenpyram is completely decomposed and mineralized into water and carbon dioxide [55]. This phenomenon also demonstrates the high mineralization ability of the prepared 2D Bi_2WO_6 photocatalyst.

On this basis, the mechanism on nitenpyram degradation by 2D Bi_2WO_6 is proposed (Fig. 7). Under visible-light irradiation, 2D Bi_2WO_6 undergoes a charge transition. Valence electrons excited by the light irradiation migrate from the valence band (VB) to the conduction band (CB); thus, photo-generated electrons and holes are generated. The h^+ in the valence band is located in the outer layer of the sandwich structure ($[BiO]^+$ layer), which can directly oxidize the nitenpyram adsorbed on the surface of the catalyst. In addition, photo-generated electrons can also react with O_2 to form superoxide radicals, which react with NTP and finally convert it to CO_2 and H_2O [58]. In addition, because of the unique layered structure of 2D layered bismuth tungstate, namely $[BiO]^+$-$[WO_4]^{2-}$-$[BiO]^+$ structure, e^- that will be left in the conduction band during the migration process $[WO_4]^{2-}$ layer causes the rapid separation of photogenerated electrons and holes. This is favorable for inhibiting their resetting and improving the photocatalytic activity of the material.

To evaluate possible photocatalytic degradation products, high-performance liquid chromatography–mass spectrometry (HPLC–MS) was used to identify the solution collected in the photocatalytic reaction (reaction solutions were pure samples with light response of 5 and 10 min).

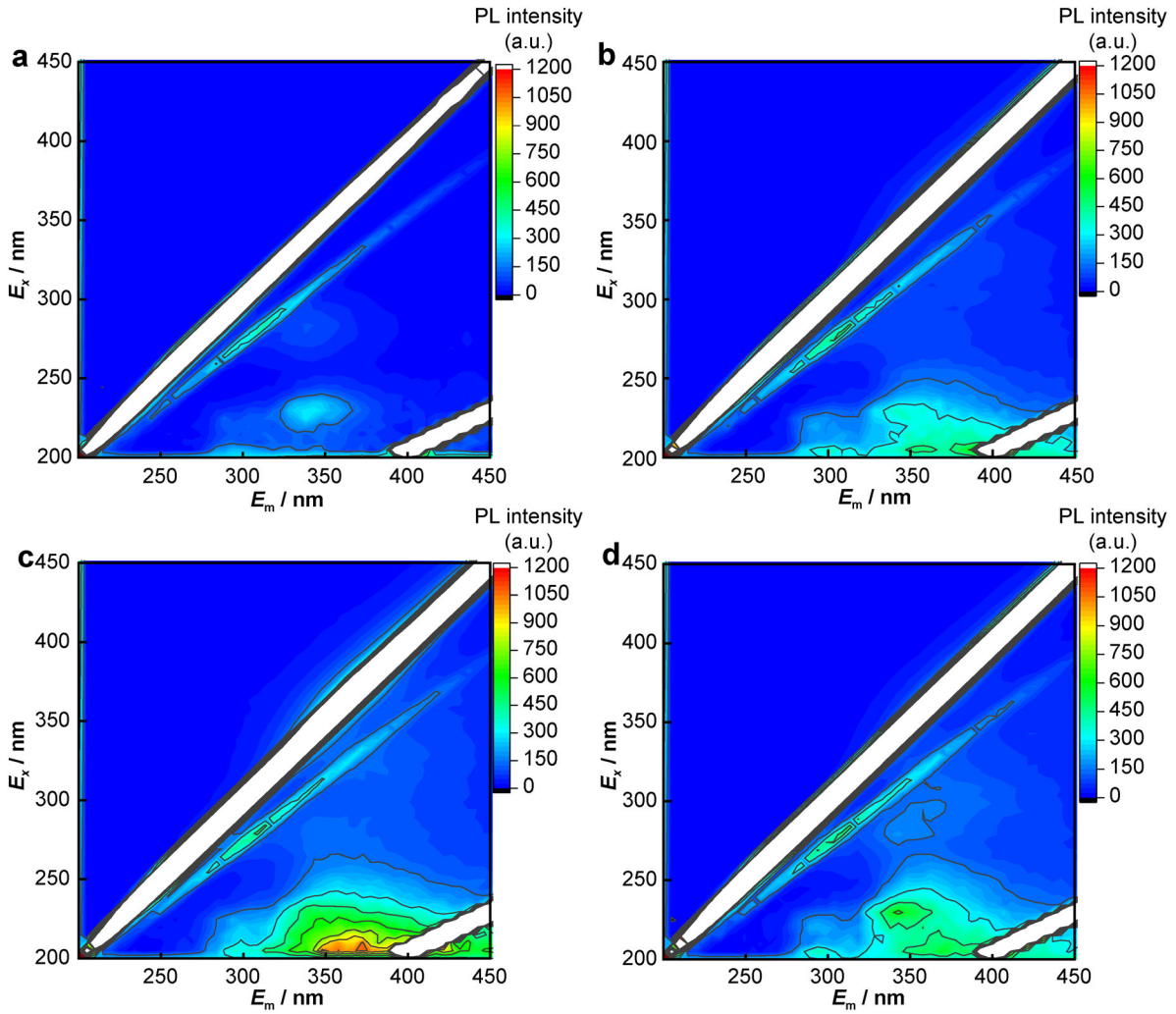

Fig. 6 **a** 3D EEMs results of original nitenpyram solution and samples obtained with visible-light irradiation time of **b** 4 min, **c** 8 min and **d** 12 min, where E_m is emission wavelength and E_x is excitation wavelength

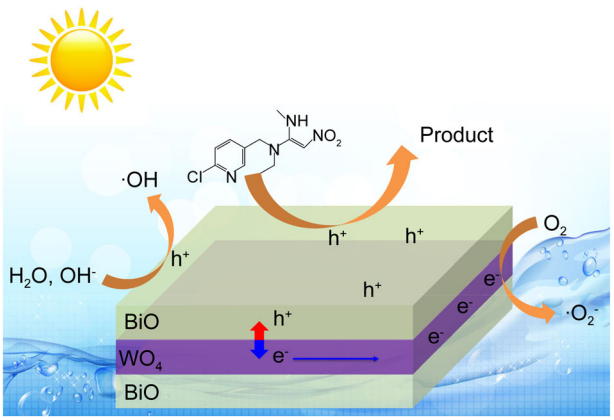

Fig. 7 Possible separated behaviors of charge carriers and photocatalytic mechanism of 2D Bi_2WO_6 for NTP degradation

According to the records of HPLC–MS, we analyzed the main intermediate structure and proposed the possible degradation pathway of nitenpyram (m/z = 270.7 g·mol^{-1}). The results are proposed in Fig. 8. There is a main peak with a mass-to-charge ratio m/z = 270.8 g·mol^{-1}, which corresponds to the nitenpyram molecule. As the reaction proceeded, NTP is oxidized and degraded into small molecules with m/z values of 223.9, 194.7, 149.7, 142.1, 116.8 and 102.1, respectively. Generally, the oxidation of organic compounds mainly occurs at the oxidation sites of organic molecules, and the oxidation sites are mainly located on functional groups. First, under the action of $\cdot O^{2-}$ and h^+, NTP falls off its methyl-linked nitro group on the side chain to form P1 (m/z = 223.9 g·mol^{-1}). With the continuous action of O^{2-} and h^+, the secondary amine bond of the branch chain breaks to form P2 (m/z = 194.7 g·mol^{-1}). And then, the groups at both ends of the tertiary amine bond of P2 are replaced to form an amine group, which forms the product P3 (m/z = 142.1 g·mol^{-1}). Finally, the branched chain is removed

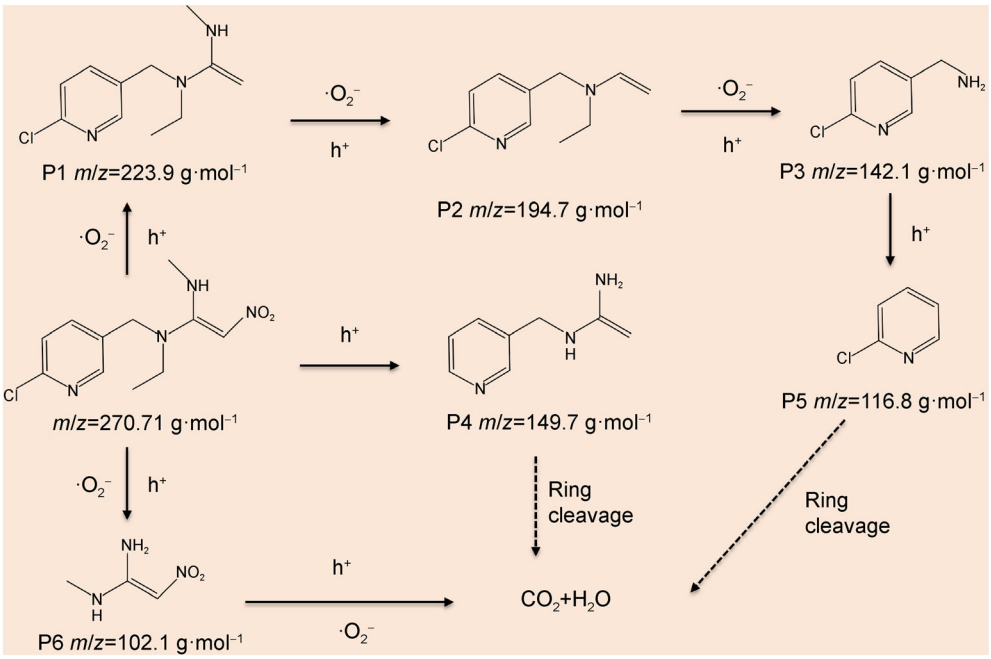

Fig. 8 Proposed possible degradation pathway of NTP in the presence of 2D Bi_2WO_6

under the oxidation of the hole h^+ to form 2-chloropyridine P5 (m/z = 116.8 g·mol^{-1}). Besides, under the oxidation of the hole, NTP may directly break the branch to form P4 (m/z = 149.7 g·mol^{-1}), or directly break the bond with the 2-chloropyridine ring to form P6 (m/z = 102.1 g·mol^{-1}). P4, P5, and P6 will be fully mineralized into CO_2 and H_2O under further degradation [40, 59, 60].

3.3 Water environment factor

The degradation reaction of NTP generally needs to be carried out in an aqueous environment. Water has the function of source and sink in the process of material migration and conversion. Therefore, it will contain various water environmental factors such as anions and cations, organic matter and heavy metal pollutants. At the same time, environmental factors, such as water level, velocity and temperature, will also increase the complexity of the water environment. These factors often have a non-negligible impact on water ecological restoration and pollution control activities. Studies have shown that the outbreak of algae in lakes is affected by temperature, wind speed and direction [61]. Similarly, when we use photocatalysts to degrade pollutants in water bodies, water environmental factors will also play an important role [62]. Our research will ultimately be devoted to environmental governance, so it is necessary to find the best conditions for photocatalytic materials to degrade pollutants by simulating the different water environmental factors, so that targeted application development is necessary. Hence, we simulated the common water environmental factors (pH, common anions, common cations and water matrix) to complete the experimental system and find the best application conditions for the material.

3.3.1 pH

The concentration of hydrogen ions (H^+) or hydroxide ions (OH^-) affects the protonation or deprotonation of pollutants and photocatalysts. Therefore, the adsorption capacity and catalytic activity of the photocatalyst will be affected by the initial solution pH [63]. In the water environment, pH is a basic water index. The original pH of the nitenpyram solution was measured to be 7.3. 0.1 mol·L^{-1} HCl solution and 0.1 mol·L^{-1} NaOH solution were used to adjust the pH to 3, 5, 7 and 9, respectively. Then, 2D Bi_2WO_6 was added to the solution, and the effect of acidity and alkalinity on the degradation reaction (experimental conditions were the same as the degradation experiment) was investigated. From Fig. 9a, it can be seen that the effect of acidity and alkalinity on the degradation of nitenpyram is not significant, all reaching more than 80%. The main effect is the adsorption stage. As shown in Fig. S4, whether it is an acidic or alkaline solution, the adsorption efficiency of nitenpyram is reduced compared to that of the original solution. This can be attributed to the

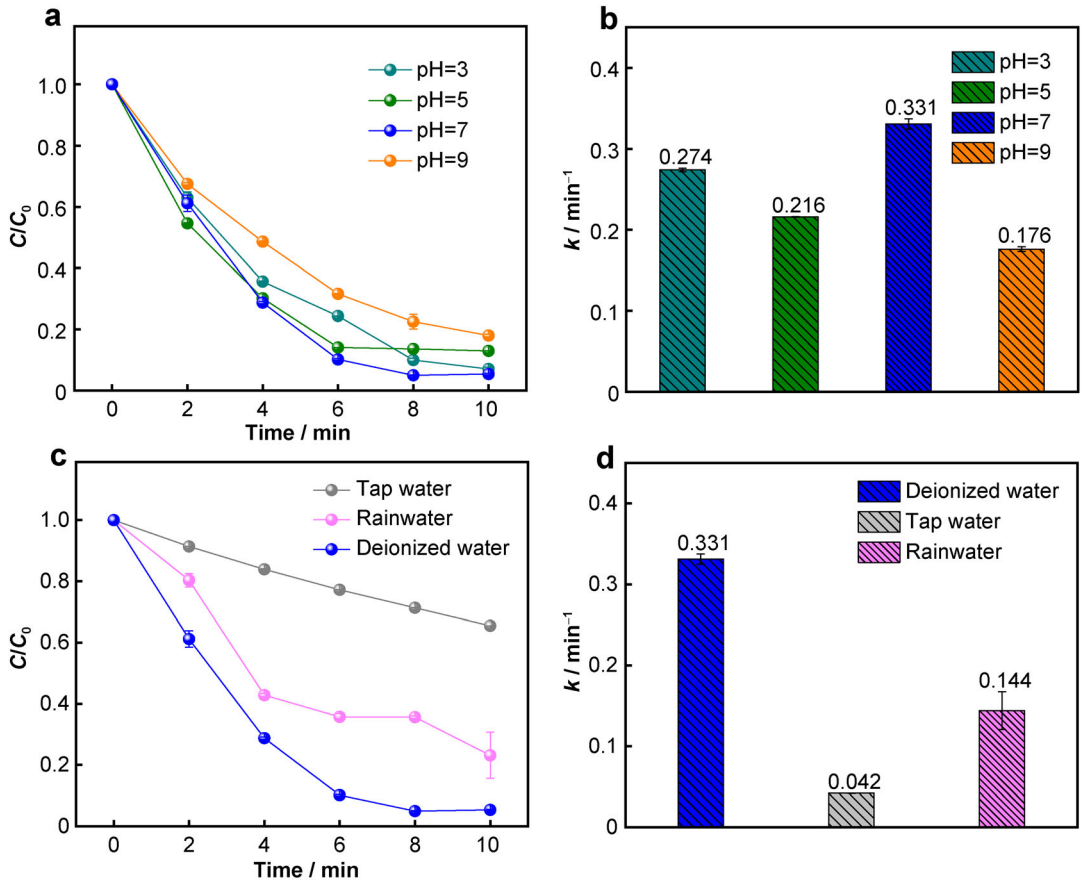

Fig. 9 **a** Degradation curves and **b** *k* values of NTP under different pH for 2D Bi_2WO_6; **c** degradation curves and **d** *k* values of NTP under different water substrates for 2D Bi_2WO_6

fact that the active sites of the unsaturated Bi atoms on the surface have competed with Cl^- and OH^-, resulting in weaker adsorption capacity. It can be seen that as the adding amount of hydrochloric acid increases, the concentration of Cl^- increases (pH 7 → 3), and the inhibition of adsorption in the dark reaction stage is enhanced. In addition, in Fig. 9b, although the degree of impact is not obvious, as the pH decreases (pH = 5 → 3), the kinetic curve constant (*k*) increases. This can be attributed to the fact that more hydrogen is absorbed on the surface of the catalyst under acidic conditions, which enhances the electropositivity of the 2D material surface layer $[BiO]^+$. Thereby, this advantage promotes the reaction between e^- and adsorbed oxygen on the surface to form $\cdot O_2^-$ ($e^- + O_2 \rightarrow \cdot O_2^-$) transfer. At the same time, it also can effectively inhibit the recombination of photogenerated electrons (e^-) and holes (h^+), so that h^+ and H_2O produce more ·OH ($h^+ + H_2O \rightarrow \cdot OH + h^+$) [56]. Also, because the two active species $\cdot O_2^-$ and ·OH have strong oxidizing properties, they promote the degradation of nitenpyram by the 2D Bi_2WO_6.

3.3.2 Water matrix

Three different water bodies, pure water, tap water, and rainwater, were selected for the photocatalytic degradation experiment of nitenpyram. The tap water source was a laboratory tap water pipe, and the rainwater came from the rainfall in Gulou District, Nanjing City on May 1st, 2020. Both tap water and rainwater have an inhibitory effect on the adsorption in the dark reaction stage. This is because both tap water and rainwater contain inorganic anions and inorganic cations, which will compete for the adsorption sites of nitenpyram (Fig. S5). In addition, as shown in Fig. 9c, d, tap water and rainwater also showed a significant inhibitory effect on the degradation of nitenpyram, and its degradation rate decreased by 60.1% and 19.5%, respectively. The reason is that tap water contained chlorinated disinfection by-products and a small amount of organic matter will combine with h^+ and ·OH, thus reducing the active substances in the reaction system [64]. In addition, we also observed that rainwater inhibited the degradation of nitenpyram to a lesser extent than tap water,

and the photoreaction did not reach the degradation equilibrium at the end. First of all, we guessed that this may be caused by the reason that the local rainwater is acidic, which has a certain promotion effect. After testing, the used rainwater is weakly alkaline, which ruled out this possibility. Therefore, we speculate that the degradation of nitenpyram may be affected by the number of bacteria and unique organic matter in the rainwater, which may require further study.

3.3.3 Common anions

Adding 5 mmol Na_2SO_4 (0.071 g), NaCl (0.0292 g), $NaNO_3$ (0.0425 g) and $NaHCO_3$ (0.042 g) to the photocatalytic reaction solution is conducted to detect the impact of common anions (SO_4^{2-}, Cl^-, NO_3^- and HCO_3^-) in the water environment. The investigated concentrations are all 0.01 mol·L^{-1}, and the pure water group is added as a control. The results are shown in Fig. 10a, b. For chloride ion, the total inhibitory effect on nitenpyram in its degradation is not obvious (degradation rate decreases by 6.3%), but the inhibition on the adsorption stage is more obvious. The reason why the adsorption effect becomes worse after adjusting the pH is that chloride ions compete for the active sites of the $[BiO]^+$ layer. In addition, some studies have shown that Cl^- inhibits the photocatalytic reaction only under acidic conditions (pH 3–4), while the degradation reaction is carried out under near neutral conditions, so the inhibition effect is not obvious. In the presence of HCO_3^-, SO_4^{2-} and NO_3^-, the degradation rate of nitenpyram is significantly lower than that of pure water, which are decreased by 52.6%, 21.6% and 17.2%, respectively. The reason may be that HCO_3^- and SO_4^{2-} are very strong scavengers for h^+ and ·OH, and the reaction formulas are as follows:

$$HCO_3^- + h^+ \rightarrow HCO_3^{\cdot -} \quad (4)$$

$$HCO_3^- + \cdot OH \rightarrow CO_3^{\cdot -} + H_2O \quad (5)$$

$$SO_4^{2-} + h^+ \rightarrow SO_4^{\cdot -} \quad (6)$$

$$SO_4^{2-} + \cdot OH \leftrightarrow SO_4^{\cdot -} + OH^- \quad (7)$$

It can be seen from the capture experiment results in Sect. 3.2 that h^+ is the main active substance involved in the photocatalytic degradation of nitenpyram. For NO_3^-, its mechanism of action is the same as that of SO_4^{2-}. In addition, the degree of hydrolysis of HCO_3^- is higher than

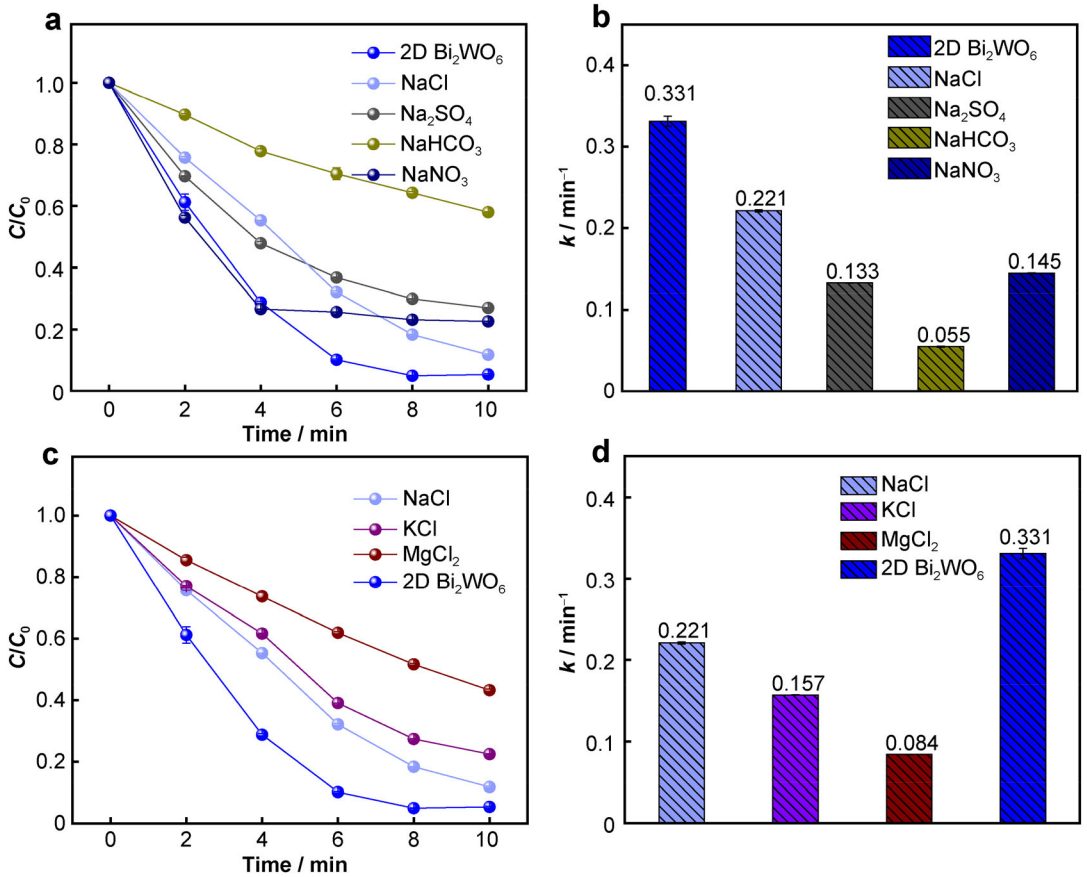

Fig. 10 **a**, **c** Degradation curves and **b**, **d** *k* values of NTP under different anions and cations for 2D Bi_2WO_6

the degree of dissociation. OH^- is also generated during the process of free radical capture, thereby increasing the pH of the reaction solution. In the above section, we know that the catalytic reaction will be inhibited to a certain extent as the pH increases. Therefore, HCO_3^- can inhibit degradation the most.

3.3.4 Common cations

We studied the influence of inorganic cations on the degradation effect of nitenpyram in the presence of Cl^-. By adding 5 mmol NaCl, KCl and $MgCl_2{\cdot}6H_2O$ to the experimental system, the cation concentration in the solution maintains at 0.01 $mol{\cdot}L^{-1}$ (adding 0.0292, 0.3725 and 0.1015 g reagents to 50 ml reaction solution, respectively). By analyzing the degradation curve (Fig. 10c, d), it is not difficult to find that the addition of K^+ and Mg^{2+} significantly inhibited the photocatalytic degradation of nitenpyram. However, the degradation rate of nitenpyram did not change much after adding Na^+ (a decrease of 6.4%). The reason may be that the radius of K^+ is larger than that of Na^+, so its adsorption to the catalyst surface occupies a large area, resulting in a smaller amount of nitenpyram adsorbed by the catalyst [65, 66]. Compared with other cations, Mg^{2+} with a higher charge has stronger electron adsorption capacity, and the decrease of electrons amount will lead to a decrease in the yield of $\cdot O_2^-$, thereby inhibiting the degradation of nitenpyram. Therefore, the addition of cations will inhibit the degradation of nitenpyram, and as the ability to add ions to absorb electrons increases, the inhibition effect increases.

4 Conclusion

In summary, 2D Bi_2WO_6 was synthesized in one-step hydrothermal method by introducing CTAB to prevent layered stacking. Meanwhile, the degradation experiments demonstrated that 2D Bi_2WO_6 has excellent NTP photocatalytic degradation ability. This is mainly due to the excellent visible-light absorption, optical carrier separation efficiency and more active sites of the layered materials. In addition, free radicals h^+ and $\cdot O_2^-$ play a major role in the degradation of NTP, which are eventually decomposed into carbon dioxide and water under the continuous attack of two active species. The study on the influence of common water environmental factors in the environment testifies to that the optimal pH is neutral, and the inhibition degree of Mg^{2+} and SO_4^{2-} is the largest, 37.8% and 52.6%, respectively. At the same time, compared with rainwater, the inhibition effect of tap water which contains more anions and anions is more obvious. This work provides a theoretical basis for the application of photocatalyst in environmental water.

Acknowledgements This study was financially supported by the National Natural Science Foundation of China (No. 51979081), the Fundamental Research Funds for the Central Universities (No. B200202103), the National Key Plan for Research and Development of China (No. 2016YFC0502203) and the National Science Funds for Creative Research Groups of China (No. 51421006) and PAPD.

Declarations

Conflict of interests The authors declare that they have no conflict of interest.

References

[1] Jiang XH, Zhang LS, Liu HY, Wu DS, Wu FY, Tian L, Liu LL, Zou JP, Luo SL, Chen BB. Silver single atom in carbon nitride catalyst for highly efficient photocatalytic hydrogen evolution. Angew Chem Int Edit. 2020;59(51):23112.
[2] Zhu M, Zhang LS, Liu SS, Wang DK, Qin YC, Chen Y, Dai WL, Wang YH, Xing QJ, Zou JP. Degradation of 4-nitrophenol by electrocatalysis and advanced oxidation processes using Co_3O_4@C anode coupled with simultaneous CO_2 reduction via SnO_2/CC cathode. Chinese Chem Lett. 2020;31(7):1961.
[3] Zhong J, Jiang H, Wang Z, Yu Z, Wang L, Mueller JF, Guo J. Efficient photocatalytic destruction of recalcitrant micropollutants using graphitic carbon nitride under simulated sunlight irradiation. Environ Sci Ecotechnol. 2021;5:100079.
[4] Schreiner VC, Link M, Kunz S, Szocs E, Scharmuller A, Vogler B, Beck B, Battes KP, Cimpean M, Singer HP, Hollender J, Schafer RB. Paradise lost? Pesticide pollution in a European region with considerable amount of traditional agriculture. Water Res. 2021;188(1):116528.
[5] Topping CJ, Aldrich A, Berny P. Overhaul environmental risk assessment for pesticides. Science. 2020;357(6476):360.
[6] Li KY, Chen J, Ao YH, Wang PF. Preparation of a ternary g-C_3N_4-CdS/$Bi_4O_5I_2$ composite photocatalysts with two charge transfer pathways for efficient degradation of acetaminophen under visible light irradiation. Sep Purif Technol. 2021;259:118177.
[7] Han WC, Tian Y, Shen XM. Human exposure to neonicotinoid insecticides and the evaluation of their potential toxicity: an overview. Chemosphere. 2018;192:59.
[8] Dai ZL, Yang WL, Fan ZX, Guo L, Liu ZH, Dai YJ. Actinomycetes rhodococcus ruber CGMCC 17550 degrades neonicotinoid insecticide nitenpyram via a novel hydroxylation pathway and remediates nitenpyram in surface water. Chemosphere. 2021;270:128670.
[9] Hladik ML, Kolpin DW. First national-scale reconnaissance of neonicotinoid insecticides in streams across the USA. Environ Chem. 2016;13(1):12.
[10] Yan S, Tian S, Meng Z, Teng M, Sun W, Jia M, Zhou Z, Bi S, Zhu W. Exposure to nitenpyram during pregnancy causes colonic mucosal damage and non-alcoholic steatohepatitis in mouse offspring: the role of gut microbiota. Environ Pollut. 2021;271:116306.
[11] Zhu L, Qi S, Xue X, Niu X, Wu L. Nitenpyram disturbs gut microbiota and influences metabolic homeostasis and immunity in honey bee (Apis mellifera L.). Environ Pollut. 2020;258:113671.

[12] Chen XC, Zhou QZ, Liu FM, Peng QR, Teng PP. Removal of nine pesticide residues from water and soil by biosorption coupled with degradation on biosorbent immobilized laccase. Chemosphere. 2019;233:49.
[13] Li SP, Jiang YY, Cao YH, Dong YW, Dong M, Xu J. Degradation of nitenpyram pesticide in aqueous solution by low-temperature plasma. Environ Technol. 2013;34(12):1609.
[14] Pang SM, Lin ZQ, Zhang WP, Mishra S, Bhatt P, Chen SH. Insights into the microbial degradation and biochemical mechanisms of neonicotinoids. Front Microbiol. 2020;11:868.
[15] Wang ZM, Shen ZY, Li YM, Zuo JL. Preparation and photoelectrocatalytic performance of Ru loaded TiO_2 nanotubes. Chin J Rare Met. 2020;44(6):609.
[16] Li JY, Ma AQ, Li HF, Dong YH, Gao YQ. Tunable micromorphology and photocatalytic properties of monoclinic $BiVO_4$ prepared by bionic template method. Chin J Rare Met. 2020; 44(9):912.
[17] Chen Y, Murakami NY, Chen HY, Sun J, Zhang QT, Wang ZF, Ohno T, Zhang M. Improvement of photocatalytic activity of high specific surface area graphitic carbon nitride by loading a co-catalyst. Rare Met. 2019;38(5):468.
[18] Zhang WD, Dong XA, Liang Y, Liu R, Sun YJ. Synergetic effect of $BiOCl/Bi_{12}O_{17}Cl_2$ and MoS_2: in situ DRIFTS investigation on photocatalytic NO oxidation pathway. Rare Met. 2019;38(5):437.
[19] Li JN, Chen J, Ao YH, Gao X, Che HN, Wang PF. Prominent dual Z-scheme mechanism on phase junction WO_3/CdS for enhanced visible-light-responsive photocatalytic performance on imidacloprid degradation. Sep Purif Technol. 2022;281:119863.
[20] Wang JF, Chen J, Wang PF, Hou J, Wang C, Ao YH. Robust photocatalytic hydrogen evolution over amorphous ruthenium phosphide quantum dots modified g-C_3N_4 nanosheet. Appl Catal B-Environ. 2018;239:578.
[21] Huang H, Zhou C, Jiao X, Yuan H, Zhao J, He C, Hofkens J, Roeffaers MBJ, Long J, Steele JA. Subsurface defect engineering in single-unit-cell Bi_2WO_6 monolayers boosts solar-driven photocatalytic performance. Acs Catal. 2020;10(2):1439.
[22] Wang Y, Liu T, Li H, Liu B, Yang L. Tungsten-based photocatalysts with UV–Vis–NIR photocatalytic capacity: progress and opportunity. Tungsten. 2019;1(4):247.
[23] Wei J, Xia Y, Qayum A, Jiao X, Chen D, Wang T. Unexpected photoinduced room temperature magnetization in Bi_2WO_6 nanosheets. Small. 2020;16(50):2005704.
[24] Ge L, Han C, Liu J. Novel visible light-induced g-C_3N_4/Bi_2WO_6 composite photocatalysts for efficient degradation of methyl orange. Appl Catal B-Environ. 2011;108–109:100.
[25] Huang H, Cao R, Yu S, Xu K, Hao W, Wang Y, Dong F, Zhang T, Zhang Y. Single-unit-cell layer established Bi_2WO_6 3D hierarchical architectures: efficient adsorption, photocatalysis and dye-sensitized photoelectrochemical performance. Appl Catal B-Environ. 2017;219:526.
[26] Liang W, Pan J, Duan X, Tang H, Xu J, Tang G. Biomass carbon modified flower-like Bi_2WO_6 hierarchical architecture with improved photocatalytic performance. Ceram Int. 2020;46(3): 3623.
[27] Zhou Y, Zhang Y, Lin M, Long J, Zhang Z, Lin H, Wu JCS, Wang X. Monolayered Bi_2WO_6 nanosheets mimicking heterojunction interface with open surfaces for photocatalysis. Nat Commun. 2015;6:8340.
[28] Kong XY, Tong T, Ng BJ, Low J, Zeng TH, Mohamed AR, Yu JG, Chai SP. Topotactic transformation of bismuth oxybromide into bismuth tungstate: bandgap modulation of single-crystalline {001}-faceted nanosheets for enhanced photocatalytic CO_2 reduction. Acs Appl Mater Inter. 2020;12(24):269919.
[29] Di J, Chen C, Zhu C, Ji M, Xia J, Yan C, Hao W, Li S, Li H, Liu Z. Bismuth vacancy mediated single unit cell Bi_2WO_6 nanosheets for boosting photocatalytic oxygen evolution. Appl Catal B-Environ. 2018;238:119.
[30] Zhang Y, Di J, Qian X, Ji M, Tian Z, Ye L, Zhao J, Yin S, Li H, Xia J. Oxygen vacancies in $Bi_2Sn_2O_7$ quantum dots to trigger efficient photocatalytic nitrogen reduction. Appl Catal B-Environ. 2021;299:120680.
[31] Zhu FY, Lv YZ, Li JJ, Ding J, Xia XH, Wei LL, Jiang JQ, Zhang GS, Zhao QL. Enhanced visible light photocatalytic performance with metal-doped Bi_2WO_6 for typical fluoroquinolones degradation: efficiencies, pathways and mechanisms. Chemosphere. 2020;252:126577.
[32] Chen Y, Li JF, Liao PY, Zeng YS, Wang Z, Liu ZQ. Cascaded electron transition in $CuWO_4$/CdS/CDs heterostructure accelerating charge separation towards enhanced photocatalytic activity. Chin Chem Lett. 2020;31(6):1516.
[33] Lu Y, Cui X, Zhao C, Yang X. Highly efficient tandem Z--scheme heterojunctions for visible light-based photocatalytic oxygen evolution reaction. Water Sci Eng. 2020;13(4):299.
[34] Yu GY, Hu FX, Cheng WW, Han ZT, Liu C, Dai Y. ZnCuAl-LDH/Bi_2MoO_6 nanocomposites with improved visible light-driven photocatalytic degradation. Acta Phys-Chim Sin. 2020;36(7):1911016.
[35] Wang B, Zhao J, Chen H, Weng YX, Tang H, Chen Z, Zhu W, She Y, Xia J, Li H. Unique Z-scheme carbonized polymer dots/$Bi_4O_5Br_2$ hybrids for efficiently boosting photocatalytic CO_2 reduction. Appl Catal B-Environ. 2021;293:120182.
[36] Yin S, Chen Y, Li M, Hu Q, Ding Y, Shao Y, Di J, Xia J, Li H. Construction of NH_2-MIL-125(Ti)/Bi_2WO_6 composites with accelerated charge separation for degradation of organic contaminants under visible light irradiation. Green Energy Environ. 2020;5(2):203.
[37] Jiang Y, Chen HY, Li JY, Liao JF, Zhang HH, Wang XD, Kuang DB. Z-Scheme 2D/2D heterojunction of $CsPbBr_3/Bi_2WO_6$ for improved photocatalytic CO_2 reduction. Adv Funct Mater. 2020; 30(50):200493.
[38] Bian XN, Zhang S, Zhao YX, Shi R, Zhang TR. Layered double hydroxide-based photocatalytic materials toward renewable solar fuels production. InfoMat. 2021;3(7):719.
[39] Zhang H, He J, Zhai C, Zhu M. 2D Bi_2WO_6/MoS_2 as a new photo-activated carrier for boosting electrocatalytic methanol oxidation with visible light illumination. Chinese Chem Lett. 2019;30(12):2338.
[40] Zhou S, Wang Y, Zhou K, Ba D, Ao YH, Wang PF. In-situ construction of Z-scheme g-C_3N_4/WO_3 composite with enhanced visible-light responsive performance for nitenpyram degradation. Chinese Chem Lett. 2021;32(7):2179.
[41] Zhang L, Yang C, Lv KL, Lu YC, Li Q, Wu XF, Li YH, Li XF, Fan JJ, Li M. SPR effect of bismuth enhanced visible photoreactivity of Bi_2WO_6 for NO abatement. Chinese J Catal. 2019; 40(5):755.
[42] Zhang YL, Zhao YC, Xiong Z, Gao T, Gong BG, Liu PF, Liu J, Zhang JY. Elemental mercury removal by I–doped Bi_2WO_6 with remarkable visible-light-driven photocatalytic oxidation. Appl Catal B-Environ. 2021;282:119534.
[43] Madriz L, Tata J, Carvajal D, Nunez O, Scharifker BR, Mostany J, Borras C, Cabrerizo FM, Vargas R. Photocatalysis and photoelectrochemical glucose oxidation on Bi_2WO_6: conditions for the concomitant H_2 production. Renew Energy. 2020;152:974.
[44] Liu YP, Shen DY, Zhang Q, Lin Y, Peng F. Enhanced photocatalytic CO_2 reduction in H_2O vapor by atomically thin Bi_2WO_6 nanosheets with hydrophobic and nonpolar surface. Appl Catal B-Environ. 2021;283:119630.
[45] Gu Q, Zhang K, Jiang P, Shen Y, Leng Y, Zhang P, Wai PT. A dual-templating strategy for synthesis of Bi_2WO_6 with oxygen vacancies for enhanced light-driven photocatalytic oxidation alcohol. Mol Catal. 2021;515:111932.

[46] Qiao Z, Liu Z, Yan W, Ruan M, Guo Z, Wu X. Pyro-photo-electric catalysis in Bi_2WO_6 nanostructures for efficient degradation of dyes under thermal-assisted visible light irradiation. J Alloy Compd. 2022;892:162203.
[47] Karbasi M, Hashemifar SJ, Karimzadeh F, Giannakis S, Pulgarin C, Raeissi K, Sienkiewicz A. Decrypting the photocatalytic bacterial inactivation of hierarchical flower-like Bi_2WO_6 microspheres induced by surface properties: experimental studies and ab initio calculations. Chem Eng J. 2022;427:131768.
[48] Wang L, Wang Z, Zhang Z, Hu C. Enhanced photoactivity of Bi_2WO_6 by iodide insertion into the interlayer for water purification under visible light. Chem Eng J. 2018;352:664.
[49] Teh YW, Goh YW, Kong XY, Ng BJ, Yong ST, Chai SP. Fabrication of Bi_2WO_6/Cu/WO_3 all-solid-state Z-scheme composite photocatalyst to improve CO_2 photoreduction under visible light irradiation. Chem Cat Chem. 2019;11(24):6431.
[50] Tauc J. Optical properties and electronic structure of amorphous Ge and Si. Mater Res Bull. 1968;3(1):37.
[51] Che HN, Gao X, Chen J, Hou J, Ao YH, Wang PF. Iodide-induced fragmentation of polymerized hydrophilic carbon nitride for high-performance quasi-homogeneous photocatalytic H_2O_2 production. Angew Chem Int Edit. 2021;60(48):25546.
[52] Tian J, Wei L, Ren Z, Lu J, Ma J. The facile fabrication of Z-scheme Bi_2WO_6-P25 heterojunction with enhanced photodegradation of antibiotics under visible light. J Environ Chem Eng. 2021;9(5):106167.
[53] Xiong X, Wang Z, Zhang Y, Li Z, Shi R, Zhang T. Wettability controlled photocatalytic reactive oxygen generation and Klebsiella pneumoniae inactivation over triphase systems. Appl Catal B-Environ. 2020;264:118518.
[54] Li M, Zhong LX, Chen W, Huang Y, Chen Z, Xiao D, Zou R, Chen L, Hao Q, Liu Z, Sun R, Peng X. Regulating the electron–hole separation to promote selective oxidation of biomass using ZnS@Bi_2S_3 nanosheet catalyst. Appl Catal B-Environ. 2021;292:120180.
[55] Deng YC, Tang L, Zeng GM, Feng CY, Dong HR, Wang JJ, Feng HP, Liu YN, Zhou YY, Pang Y. Plasmonic resonance excited dual Z-scheme $BiVO_4$/Ag/Cu_2O nanocomposite: synthesis and mechanism for enhanced photocatalytic performance in recalcitrant antibiotic degradation. Environ Sci-Nano. 2017;4(7):1494.
[56] Ao YH, Xu LX, Wang PF, Wang C, Hou J, Qian J. Preparation of CdS nanoparticle loaded flower-like $Bi_2O_2CO_3$ heterojunction photocatalysts with enhanced visible light photocatalytic activity. Dalton T. 2015;44(25):11321.
[57] Mu RH, Ao YH, Wu TF, Wang C, Wang PF. Synthesis of novel ternary heterogeneous anatase-TiO_2 (B) biphase nanowires/$Bi_4O_5I_2$ composite photocatalysts for the highly efficient degradation of acetaminophen under visible light irradiation. J Hazard Mater. 2020;382:121083.
[58] Zhao Y, Wang Y, Liu E, Fan J, Hu X. Bi_2WO_6 nanoflowers: an efficient visible light photocatalytic activity for ceftriaxone sodium degradation. Appl Surf Sci. 2018;436:854.
[59] Xu J, Chen J, Ao Y. 0D/1D AgI/MoO_3 Z-scheme heterojunction photocatalyst: highly efficient visible-light-driven photocatalyst for sulfamethoxazole degradation. Chinese Chem Lett. 2021;32(10):3226.
[60] Tang ML, Ao YH, Wang PF, Wang C. All-solid-state Z--scheme WO_3 nanorod/$ZnIn_2S_4$ composite photocatalysts for the effective degradation of nitenpyram under visible light irradiation. J Hazard Mater. 2020;387:121713.
[61] Zhang WL, Li Y, Su YL, Mao K, Wang Q. Effect of water composition on TiO_2 photocatalytic removal of endocrine disrupting compounds (EDCs) and estrogenic activity from secondary effluent. J Hazard Mater. 2012;215–216:252.
[62] Zhang C, Li Y, Li MQ, Shuai DM, Zhou XY, Xiong XY, Wang C, Hu Q. Continuous photocatalysis via photo-charging and dark-discharging for sustainable environmental remediation: performance, mechanism, and influencing factors. J Hazard Mater, 2021;420:126607.
[63] Hu PD, Long MC. Cobalt-catalyzed sulfate radical-based advanced oxidation: a review on heterogeneous catalysts and applications. Appl Catal B-Environ. 2016;181:103.
[64] Lin JW, Hu YY, Wang LX, Liang DH, Ruan X, Shao SC. M88/PS/Vis system for degradation of bisphenol A: environmental factors, degradation pathways, and toxicity evaluation. Chem Eng J. 2020;382:122931.
[65] Huang Y, Nengzi LC, Zhang XY, Gou JF, Gao YJ, Zhu GX, Cheng QF, Cheng XW. Catalytic degradation of ciprofloxacin by magnetic CuS/Fe_2O_3/Mn_2O_3 nanocomposite activated peroxymonosulfate: influence factors, degradation pathways and reaction mechanism. Chem Eng J. 2020;388:124274.
[66] Ma XH, Zhao L, Dong YH. Oxidation degradation of 2,2′,5-trichlorodiphenyl in a chelating agent enhanced Fenton reaction: influencing factors, products, and pathways. Chemosphere. 2020;246:125849.